J Electroceram (2006) 17:211–219
DOI 10.1007/s10832-006-7537-0

Interface mediated transport properties in n-type $SrTiO_3$: Induced dipole alignment at oxide grain boundaries

Rui Shao · Dawn A. Bonnell

Received: 29 August 2005 / Revised: 12 January 2006 / Accepted: 31 January 2006

Abstract Low temperature potentiometry and capacitance measurements based on noncontact atomic force microscopy were used to quantify local properties due to grain boundaries at a 0.05 wt.% Nb-doped $SrTiO_3$ [001] surface. Local *I-V* curves were constructed by combining potential steps and transport currents measured at individual grain boundaries (GBs) under different lateral biases. The GBs exhibit a positive temperature coefficient of resistivity (PTCR) effect. A comparison of transport properties and calculations suggest that $SrTiO_3$ grain boundaries undergo a non-polar to polar state phase transition induced by the large electric field associated with the boundary charge. This is supported by the temperature dependence of the barrier height and the boundary charge obtained by numerical simulation of *I-V* curves using a double Schottky barrier model. The built-in potential associated with the boundary was directly imaged with frequency-modulated Kelvin probe force microscopy at different temperatures and the results support the previous conclusion.

Keywords Grain boundary · Atomic force microscopy · Positive temperature coefficient of resistivity

1 Introduction

Transport in electronic metal oxides is often limited by resistive grain boundaries (GBs), which give rise to the so-called varistor behavior [1]. The perovskite-type oxides exhibit even more important GB effects, such as positive temperature coefficients of resistivity, low field magnetoresistivity, and lowered critical current density in the superconducting state. All of these phenomena are ascribed to the space charge near the interface.

The boundary charge is strongly dependent on the structure, thermal history and composition. To determine the structural origin of the boundary charge, electron microscopy, local electron energy loss spectroscopy as well as first principle calculations have been used to characterize special $SrTiO_3$ bicrystals, which are often regarded as a model [2–4]. Not until recently have low temperature transport results been reported on these model interfaces [5–8]. Given the ideality of the geometry of a bicrystal, traditional four-point transport measurements are good enough for characterizing the effect of GBs on *I-V* properties; however, direct observation of boundary charge requires scanning tunneling microscopy and several other scanning probe techniques.

Although scanning probe measurements of boundary charge and the dynamic behavior of individual GBs were demonstrated [9, 10], the magnitude of the potential related to the boundary charge was found to be substantially smaller than that determined from transport measurements. In some cases, the sign of the measured potential is even opposite to that expected from the band structure model [10, 11]. These complications may be rationalized in terms of charge screening by adsorbates in the ambient environment. In addition, ambient surface potentiometry (or Kelvin probe force microscopy) is implemented in lift mode, which suffers from averaging effect and yields reduced resolution as the tip-sample separation increases.

In this paper, we present a systematic study of the dc transport properties in donor-doped high angle $SrTiO_3$ GBs at low temperatures using two scanning potentiometric techniques, as well as scanning impedance microscopy implemented in

R. Shao · D. A. Bonnell (✉)
Department of Materials Science and Engineering,
University of Pennsylvania, 3231 Walnut Street, Philadelphia,
PA 19104
e-mail: bonnell@seas.upenn.edu

ultra-high vacuum (UHV) condition. UHV is required to produce clean sample surfaces that can be cooled down free from moisture condensation. This paper also presents the observation of the low temperature positive temperature coefficient of resistivity (PTCR) effect at $SrTiO_3$ GBs.

2 Potential barriers in donor-doped grain boundaries

Interface trap states in electroactive donor-doped GBs result in boundary charge and adjacent depletion regions with low carrier concentrations. The band structure of such an electroactive *GB* is depicted in Fig. 1(a). Potential within the depletion regions causes upward band-bending to form a double Schottky barrier (DSB) with barrier height φ_{GB}. Using abrupt junction approximation, the depletion width d is related to the boundary charge density Q_{GB} (in m^{-2}) and donor concentration N_D (in m^{-3}, and assuming complete ionization) by

$$Q_{\mathrm{GB}} = 2N_{\mathrm{D}}d. \tag{1}$$

Thus the unit area boundary capacitance C_{GB} (in F/m^2) is given by

$$C_{GB} = \frac{\varepsilon_r^{GB}\varepsilon_0}{d} = \frac{2\varepsilon_r^{GB}\varepsilon_0 N_D}{Q_{GB}}, \tag{2}$$

where $\varepsilon_r^{\mathrm{GB}}$ is the relative dielectric constant of the boundary and $\varepsilon_0 = 8.85 \times 10^{-12}$ F/m.

Under lateral bias V, the interface charge increases to $Q(V)$ and barrier height decreases to $\varphi_{GB}(V)$ (Fig. 1(b)). $\varphi_{GB}(V)$ and $Q_{GB}(V)$ are related by

$$Q_{\mathrm{GB}}(V) = \sqrt{\frac{\varphi_{GB}(V)}{4\gamma}} + \sqrt{\frac{\varphi_{GB}(V) + eV}{4\gamma}}, \tag{3}$$

where $e = 1.6 \times 10^{-19}$ C and $\gamma = e^2/8\varepsilon_0\varepsilon_r^{GB}N_D$, assuming the boundary density of states is uniformly distributed in energy. According to the formulation proposed by Pike et al. [12], the boundary charge is related to the Fermi level of the bulk E_{FB}, the Fermi level of the "boundary phase" E_{BV} and $\varphi_{GB}(V)$ by

$$Q_{GB}(V) = N_T(E_{FV} - E_{BV} - \varphi_{GB}(V) - eV_1) \tag{4}$$

where $eV_1 = -kT\ln[\frac{1+\exp(-eV/kT)}{2}]$, N_T is the density of states, and $k = 1.38 \times 10^{-23}$ J/K. $Q_{GB}(V)$ and $\varphi_{GB}(V)$ can be numerically solved from Eqs. (3) and (4). With a known $\varphi_{GB}(V)$, the *I-V* characteristics within the thermionic emission model is $J = A^*T^2\exp(-\frac{e\varphi_{GB}(V)}{kT})[1 - \exp(-\frac{eV}{kT})]$.

In principle, a nonlinear least square (NLS) fitting of experimental *I-V* curves yields Q_{GB} and φ_{GB} at different temperatures. In order to use this approach, precise knowledge of the temperature dependence of ε_r^{GB} is needed, since it is clear from Eq. (3) that Q_{GB} is dependent on ε_r^{GB}. As is well known the dielectric constant in $SrTiO_3$ single crystals, ε_r, exhibits typical paraelectric behavior and follows the Curie-Weiss law [13]

$$\varepsilon_r = \frac{8 \times 10^4}{T - 35.5} \tag{5}$$

As the temperature decreases from 300 K to 40 K, ε_r increases from 300 to several thousands. However, it is problematic to assume that ε_r^{GB} is identical to ε_r. Previous studies have shown that the dielectric constant in polycrystalline $SrTiO_3$ is much more suppressed at low temperatures than in a single crystal [5, 14, 15]. On the other hand, ε_r^{GB} can only be deduced from C_{GB}, which is the physical quantity directly measurable. In addition, as seen from Eq. (2), C_{GB} is also a function of *GB* charge Q_{GB}, which could also vary with temperature. Here we propose a self-consistent method to solve this problem. At a given temperature, ε_r^{GB} is assigned the value calculated from Eq. (5), i.e., the *GB* dielectric constant is assumed to be the same as that of the bulk. Next Q_{GB} and φ_{GB} are obtained by NLS fitting of the *I-V* curve. Then a new value of ε_r^{GB} is calculated from Eq. (2) and is used in the next iteration of NLS fitting. The fitting stops when convergence of ε_r^{GB} is achieved. It is to be noted that, in this work, ε_r^{GB} is assumed to be field independent to the first order approximation. A more accurate analysis, of course, should treat ε_r^{GB} as $aE + bE^2$, where a and b are linear and nonlinear factors.

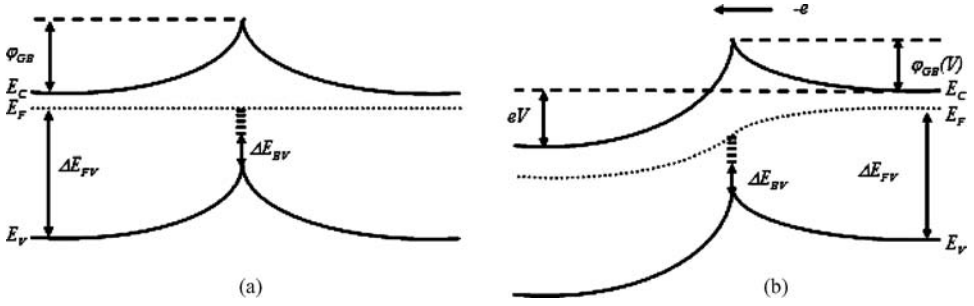

Fig. 1 Band structure of the GB under zero bias (a) and non-zero lateral bias V (b). The boundary is negatively charged due to trap states

3 UHV electrical scanning probe microscopy

Kelvin probe force microscopy (KPFM) in UHV is based on frequency modulation and detection in noncontact atomic force microscopy (NC-AFM) [16]. This is generally referred to as frequency modulated KPFM (FM-KPFM). An electrical bias $V_{tip} = V_{dc} + V_{ac}\cos\omega t$ is applied to the conductive NC-AFM tip. The resonant frequency shift Δf_r induced by the capacitive force between the tip and the surface at potential V_s is given by

$$\Delta f_r = -K(V_{tip} - V_s)^2, \tag{6}$$

where K is a factor expressed in terms of the resonance of a free oscillating cantilever f_0, its spring constant k, and the derivative of tip-surface capacitive gradient $\partial^2 C/\partial z^2$ as $K = \frac{1}{2}\frac{f_0}{k}\frac{\partial^2 C}{\partial z^2}$. The Δf_r contains oscillating components of both 1ω and 2ω harmonics. The amplitude of the $1\ \omega$ harmonic $\Delta f_{1\omega} = -K(V_{dc} - V_s)V_{ac}$ is nullified by a feedback by adjusting V_{dc} to V_s.

Alternatively, V_s can be measured in NC-AFM mode in a manner of point spectroscopy, which is to collect $\Delta f_r(V_{tip})$ curves at different locations and fit them to a 2nd order polynomial, since, according to Eq. (6), $\Delta f_r(V_{tip})$ is a quadratic function with the maximum at $V_{tip} = V_s$. This method was recently applied to profiling the potential step across a laterally biased $SrTiO_3$ *GB* [17].

Scanning impedance microscopy (SIM) is implemented with the cantilever scanning above the surface at a finite tip/surface separation without being mechanically oscillated. As shown in Fig. 2, an ac bias $V_{ac}cos\omega t$ is applied to the sample interface connected in series with two current limiting resistors R. By modeling the interface as a parallel RC circuit with parameters R_i and C_i, the potential on the left and right side of the interface are in the form [18]

$$V_L = A_L\cos(\omega t + \varphi_L) \quad \text{and} \quad V_R = A_R\cos(\omega t + \varphi_R). \tag{7}$$

In Eq. (7), amplitudes A_L, A_R and phases φ_L, φ_R are quantitatively connected by the interface impedance

$$Z_i = 1/(1/R_i + j\omega C_i) \quad \text{as} \quad A_L/A_R = \left|1 + \frac{1}{RZ_i}\right| = \left|1 + \frac{1}{R(1/R_i + j\omega C_i)}\right| \tag{8}$$

and

$$\Delta\varphi = \varphi_L - \varphi_R = -\arctan\left(\frac{\omega C_i R_i^2}{R + R_i + \omega^2 C_i^2 R_i^2 R}\right), \tag{9}$$

where $j = \sqrt{-1}$. In the limit of high frequency $\omega >> 1/R_iC_i$, Eqs. (8) and (9) are simplified to $A_L/A_R = 1$, and

$$\Delta\varphi = -\arctan\frac{1}{\omega RC_i}. \tag{10}$$

When the tip is biased at V_{dc}, a cantilever oscillation is induced by the electrostatic force $F = -\frac{1}{2}\frac{\partial C}{\partial z}\{V_{dc} - V_s - V(x)\cos[\omega t + \varphi(x)]\}^2$, where x is the lateral distance from the interface. The $1\ \omega$ component of the mechanical oscillation, which is detected with a lockin amplifier, is proportional to $F_{1\omega} = \frac{\partial C}{\partial z}(V_{dc} - V_s)V(x)\cos[\omega t + \varphi(x)]$. Thus the phase difference in the tip oscillation as the tip is scanned across the interface is given by Eq. (9). In the high frequency limit, it is given by Eq. (10), from which C_i can be quantified when ω and R are known.

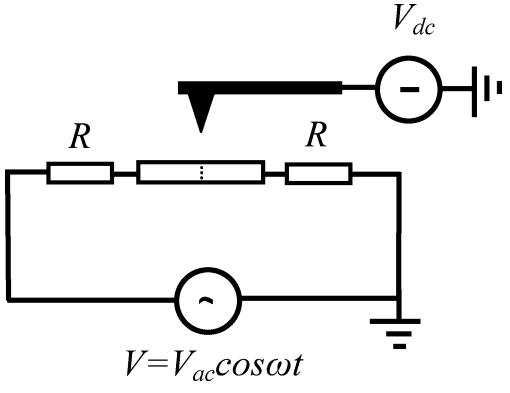

Fig. 2 Experimental setup of scanning impedance microscopy on an electroactive interface: A conductive cantilever without mechanical oscillation is scanned above an interface with maintained tip/surface separation; a dc bias is applied to the cantilever and an ac bias is applied to the interface connected in series with two current limiting resistors R

4 Experimental procedures

All measurements were performed in a UHV variable temperature AFM system (Omicron Nanotechnology) with a base pressure lower than 7.1×10^{-11} torr. The sample stage of the microscope and feed-throughs were modified to apply lateral biases. Two chemical-mechanically polished 0.05 wt% Nb doped $SrTiO_3$ bicrystal slabs ($10 \times 1.6 \times 0.5$ mm^3) with 24° [001] symmetric tilt GB in the middle were used. These samples were sectioned from one $10 \times 10 \times 0.5$ mm^3 bicrystal with a diamond saw. Carrier concentration was $1.1 \times 10^{25}\ m^{-3}$, as determined from Hall effect measurement. Z-contrast imaging in transmission electron microscopy on these samples confirms the absence of second phase segregation or other impurities. GB resistance in both as-received samples was 30 MΩ as determined by two point probe measurement.

Table 1 Comparison of Sample A and Sample B

	Annealing	φ_{GB} at 300 K	T_{MAX} (K)	T_C (K)
Sample A	No	0.36 eV	≈240 K	≈200 K
Sample B	(1) 1000°C in UHV, 10 min (2) 750°C in air, 2 h	0.10 eV	40 K	<40 K

Immediately before being transferred to the sample stage for SPM measurements, both Samples A and B were heated in UHV at about 300°C for 3 h to desorb moisture. No extra processing was done on Sample A. Sample B was then annealed at 1000°C by dc heating for 10 min in UHV and was taken out for low temperature four-point *I-V* measurements in a helium dewar. Six narrow, equally spaced indium contacts were soldered onto the Sample B surface (three on each side of the GB) to facilitate *I-V* measurement both across the GB and on the bulk single crystal. Indium contacts were then completely removed with care taken to avoid damage to the surface near the GB. Subsequently, Sample B was annealed in air at 750°C for 2 h and transferred into the UHV chamber for SPM study. A comparison of Sample A and B is listed in Table 1.

A Pt/Ir coated cantilever (PPP-EFM, $k \approx 1\sim3$ N/m, $f_0 = 55$ kHz) was used for NC-AFM measurement. A lockin amplifier and feedback controller (SRS830, SIM960, Stanford Research Systems) were used in the homebuilt circuits for FM-KPFM and SIM measurements. A function generator (DS340, Stanford Research Systems) and multimeter (K2000, Keithley) were used to apply sample bias and monitor the transport current. Temperature control was achieved with liquid He or N_2 in the cryostat and adjusting the power of a built-in heater. In FM-KPFM the ac drive voltage V_{ac} was set to 0.5 V_{rms} and 1 kHz, and the setpoint was maintained at −15 Hz. For SIM, the lateral ac bias was 0.15 Vrms at $\omega = 90$ kHz. The tip was biased at −1 V when scanning at very slow rate, 0.1 Hz. The tip/sample distance was maintained at 50 nm.

5 Results and discussion

5.1 dc and ac transport dynamics of the GB

The presence of a highly resistive *GB* is evident from the step in the surface potential profile of Sample A under external bias V_{EXT} (Fig. 3(a)). As shown in Fig. 3(b), the voltage step across the *GB* V_{LAT} increases with V_{EXT} and exhibits breakdown behavior when V_{EXT} exceeds 1.2 V. At temperatures between 90 K and 319 K, using V_{LAT} and the current I measured simultaneously, local *I-V* curves were constructed, which show typical varistor behavior with nonlinearity $\alpha = \partial \ln(I)/\partial \ln(V_{GB})$ in the range of 4.5 to 6.9 at high biases. The GB exhibits more interesting behavior in the temperature dependence of the resistance R_{GB} calculated

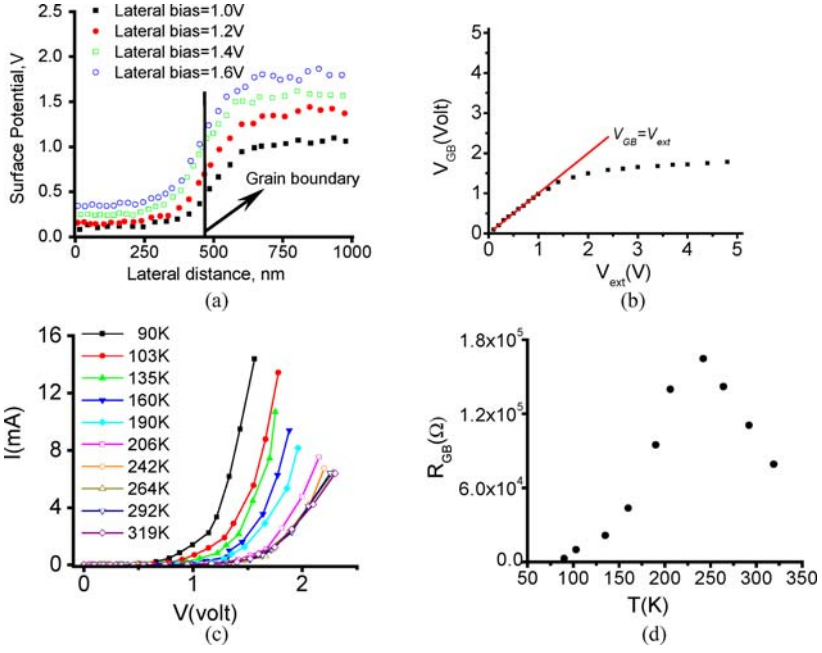

Fig. 3 (a) Local potential steps across the grain-boundary under different lateral biases. (b) The measured potential difference V_{GB} is comparable with the externally applied lateral bias V_{ext} at low biases, but is much smaller at high voltages, indicting a breakdown behavior of the potential barrier. The breakdown voltage is around 1.2 V. (c) Local I-V characteristics from 90–319 K constructed with current I measured by a multimeter and V_{GB}. (d) *GB* resistance at difference temperatures calculated from the local I-V curves shows the typical PTCR behavior

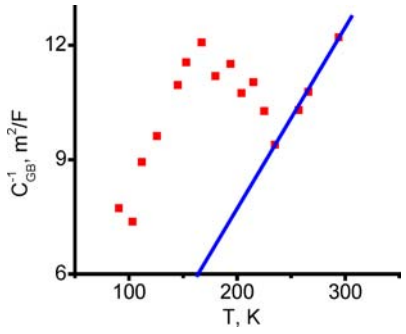

Fig. 4 Temperature dependence of the reciprocal capacitance of the *GB* C_{GB}^{-1} measured with SIM. C_{GB}^{-1} follows Curie-Weiss law (solid line) above 235 K and significantly deviates below this temperature indicating a possible onset of phase transition

at $V_{LAT} = 0.08$ V. As the temperature decreases, R_{GB} first increases by 3 times to a maximum with corresponding temperature $T_{\mathrm{MAX}} = 240 \pm 25$ K, and then declines by two orders of magnitude. The boundary capacitance C_{GB} was measured at different temperatures by SIM. As shown in Fig. 4, the temperature dependence of reciprocal capacitance C_{GB}^{-1} follows the Curie-Weiss law, i.e. $C_{GB}^{-1} \propto T - T_0$, above 235 K, where $T_0 = 40.4$ K. A significant deviation from Curie-Weiss law occurs upon further cooling down, implying a possible phase transition at the boundary. The observations of resistance and capacitance anomalies are reminiscent of the positive temperature coefficient of resistivity (PTCR) effect well studied in donor-doped $BaTiO_3$ and $Ba_xSr_{1-x}TiO_3$ ceramics [19–21]. In PTCR ceramics, the resistance decreases rapidly when T drops below T_C as a result of boundary charge being compensated by adjacent ferroelectric domains.

To further clarify the basis of the *R-T* dependence, the analysis outlined in Section 2 was applied to the transport data. The fitted curves in Fig. 5(a) are used to extract the parameters shown in Fig. 5(b). As T decreases from 319 K, φ_{GB} slowly decreases initially until around 200 K, a sharper decrease occurs accompanied by a decrease Q_{GB}. Such behavior fits well with the picture of a PTCR model, indicating a possible ferroelectric ordering at the GB. This is further supported by the temperature dependence of ε_r^{GB}obtained from the NLS fitting. Compared to the paraelectric behavior predicted by Eq. (5), ε_r^{GB} is much smaller at below 250 K. Such a low temperature suppression in ε_r^{GB} was explained by Petzelt et al. in terms of polar phase in the vicinity of the GB [5].

It was well known that bulk $SrTiO_3$ is not ferroelectric. Besides a structural transition at 105 K from cubic to tetragonal, $SrTiO_3$ also undergoes a phonon anomaly around 35 K and becomes an incipient ferroelectric, in which quantum fluctuation disrupts the formation of stable domains. However, a ferroelectric-like phase transition involving dipole alignment can be induced by strong electric field [22]. At $T =$ 293K, $Q_{GB} = 7.6 \times 10^{17}$ m^{-2} and $\varphi_{GB} = 0.36$ eV. Thus the depletion width $d = Q_{GB}/2N_d = 34.5$ nm and the average field $\bar{E} = \varphi_{GB}/e/d = 10^4\, V/\mathrm{mm}$. Calculation by Hemberger et al. shows that the critical phase transition temperature increases with the magnitude of field and that 600 V/mm is sufficient to polarize bulk $SrTiO_3$ at about 37 K. As will be shown later, the transition temperature in this sample should be significantly higher due to the much stronger field. Based on the temperature dependence of Q_{GB} and φ_{GB}, the transition temperature T_C for Sample A should be around 200 K. Although, in a strict sense ferroelectricity requires switchability of dipoles and switching of the polar region near the *GB* cannot be achieved due to the limitation on sample geometry and finite conductivity, the formation of the polar region is clearly of the same nature as induced ferroelectric state in $SrTiO_3$.

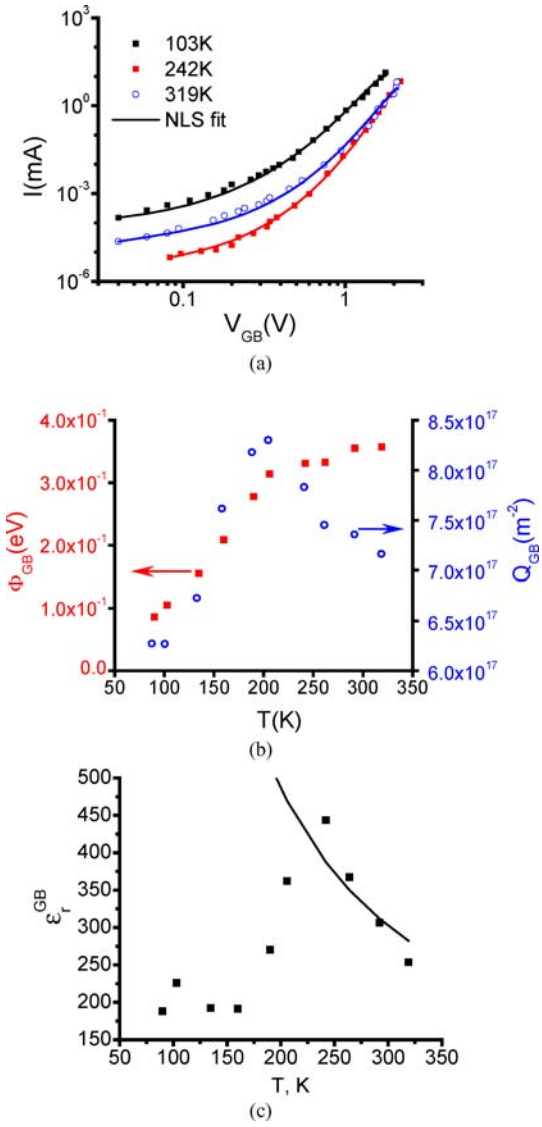

Fig. 5 (a) Experimental *I-V* curves were fitted with NLS fitting to numerical simulations. (b) temperature dependence of Q_{GB} and φ_{GB}. (c) temperature dependence of ε_r^{GB} and its comparison to Curie-Weiss law (solid curve)

Furthermore, as shown in Fig. 6, a 24° boundary structure consists of periodic structural units. Each period contains in

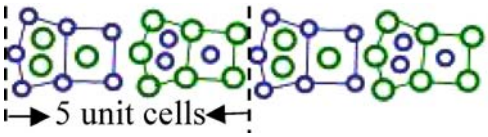

Fig. 6 Atomic structure of the dislocation core of a 24° [001] tilt $SrTiO_3$ *GB* viewed along, which consists of repeated structure units each in the form of "Pentagon"-distorted unit cell-"Pentagon"- distorted unit cell. Large circles are Sr columns and small circles are Ti-O columns

order a Ti pentagon, distorted Ti unit cell, Sr pentagon, and a distorted Sr unit cell, where Ti and Sr refer to the cations in the vertices of either the "pentagon" or "distorted unit cell" [8]. Given the boundary structure, it is instructive to estimate the charge density per periodic structural unit Q_{SU}. At 293 K, Q_{GB} is 7.4×10^{17} m^{-2} and the area of one structural unit S is 5 unit cells, i.e. $S = 0.4 \times 0.4 \times 5 = 0.8$ nm^2. So $Q_{SU} = Q_{GB} \times S = 0.6$ electron. The same analysis on a 36.8 degree boundaries, which consist of the same sub units in a different order yields a similar number suggesting that a general conclusion is that these periodic units contain around 1 electron each.

5.2 Effect of high temperature annealing on GB charge

High temperature annealing dramatically changed the conductivity of the *GB*, as seen from the four-point measurements between 1.4 K and 290 K. In a broad temperature range from 65 to 290 K, the four-point *I-V* curves both across the *GB* and on the bulk are linear. R_{GB} follows the same trend as the bulk resistance, which means that the *GB* effect is nonexistent (Fig. 7(a)). Below 65 K, the trend of *GB* resistance resembles a metal to insulator transition. The nonlinearity of the *GB* IV curves becomes detectable below 30 K (Fig. 7(b)). Measured *dI/dV* curves at low temperatures follow $dI/dV \propto V^2$ well, which is consistent with elastic tunneling of electrons across a thin insulating region between two similar metal electrodes [23]. However, a closer look at the zero bias region of the curves shows a deviation from V^2 dependence (Fig. 7(c)). A better fit in this region is $V^{0.5}$, which suggests that the transport contains a slight contribution from tunneling through a charge disordered region, as reported on reduced, undoped bicrystals [7]. This transport mechanism is consistent with the metal-to-insulator like transition exhibited in the temperature dependence of GB resistance, because disorder induces weak localization of charge. These results show that reduction decreases the *GB* charge. Further supporting evidence is that annealing in air for 2 h restored the boundary charge to some extent. Apparently oxygen plays an important role in the formation of *GB* charge.

5.3 Direct imaging of *GB* charge

While point-spectroscopy is effective in quantifying the potential difference across the laterally biased interfaces, it does not provide the spatial resolution necessary to directly image the potential variation associated with the *GB* depletion region, which is typically tens of nanometers in width. We performed simultaneous NC-AFM and FM-KPFM measurements on Sample B to image the topography and the potential profiles of the *GB* under different biases. In the topographic image of the boundary unit cell height steps on both sides of the boundary run primarily along {120} direction (Fig. 8(a)). The FM-KPFM images acquired at 293 K (Fig. 8(b)–(d)) shows that the built-in potential $V_{GB} = -\varphi_{GB}/e$ in the depletion region is negative as is expected from the fact that the boundary is negatively charged. The magnitude of V_{GB} is around -97 ± 6 mV under zero lateral bias. Using an abrupt junction approximation, the depletion width d and average field $\bar{E}$ as calculated from $V_{GB} = \frac{eN_d d^2}{2\varepsilon_r \varepsilon_0}$ are 18 nm and 5500 V/mm.

When a positive lateral bias V is applied on the left grain, the barrier height decreases in magnitude. From Eq. (3), the barrier heights at zero bias $\varphi_{GB}(0)$ and bias V, $\varphi_{GB}(V)$ are

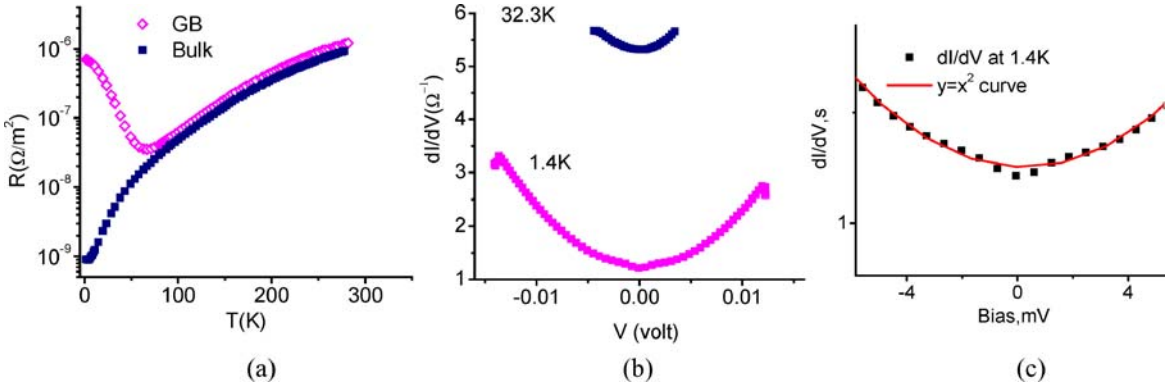

Fig. 7 (a) The *GB* and the bulk resistances of the reduced 24° bicrystal. (b) *dI/dV* curves measured at 1.4 K and 32.3 K show nonlinear transport characteristic of electron tunneling between similar electrodes across an insulating gap. (c) Zoom-in on the zero bias region of *dI/dV* curve at 1.4 K and the fit to $y = x^2$

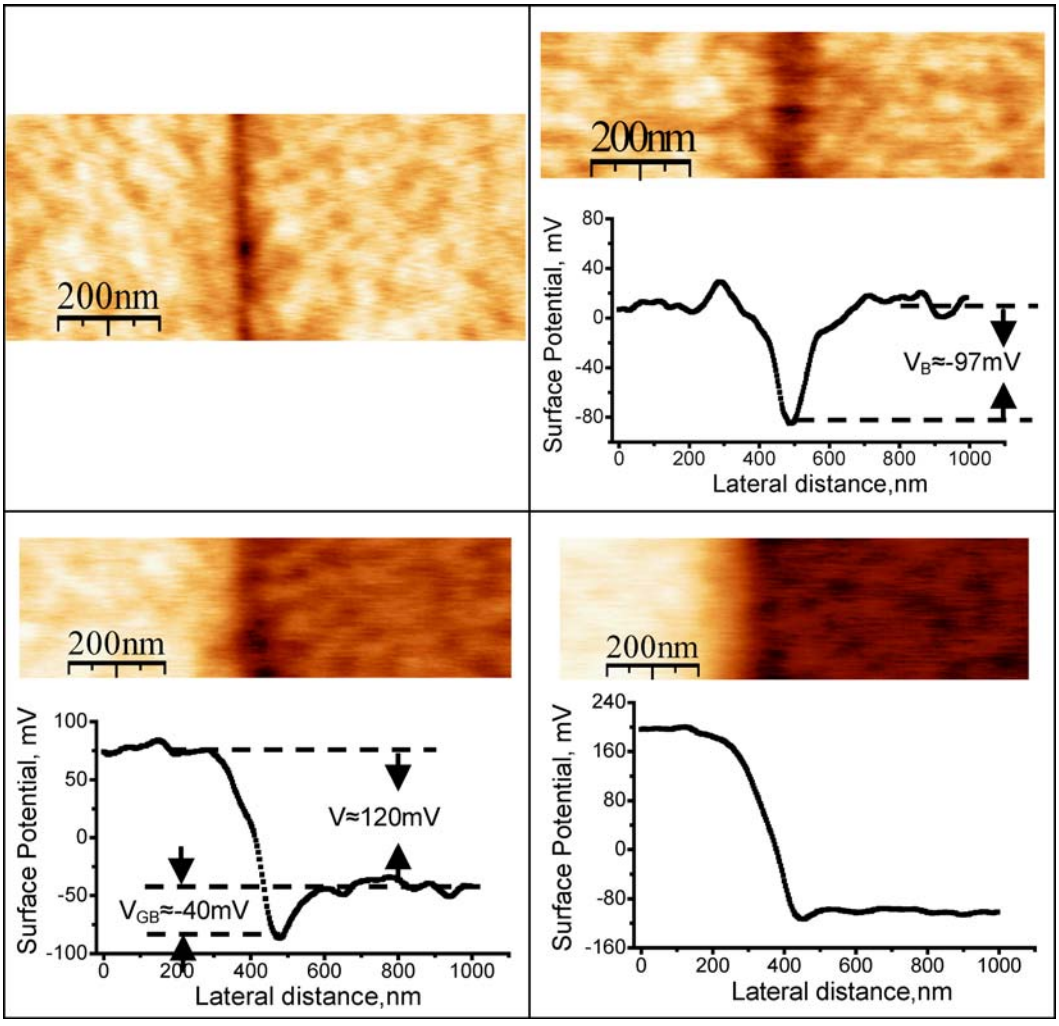

Fig. 8 Direct visualization of the *GB* topography and built-in potential V_{GB} by simultaneous NC-AFM and FM-KPFM imaging on Sample B: (a) topography by NC-AFM, unit steps on both sides of the *GB* groove are symmetric and predominantly run along {120} direction. (b) under zero bias, V_{GB} is around −100 mV. (c) under the lateral bias of 120 mV applied on the left side, V_{GB} decreases in magnitude to around −40 mV. (d) under even lateral bias of 300 mV, V_{GB} further decreases in magnitude to around −10 mV, close to flat band condition

related by

$$\varphi_{GB}(V) = \varphi_{GB}(0)k^2\left[1 - \frac{eV}{4k^2\varphi_{GB}(0)}\right]^2, \qquad (11)$$

where $k = Q(V)/Q(0)$, the ratio of boundary charges at bias V and zero, is close to one at low biases. With the lateral bias V from the potential profile, $\varphi_{GB}(V)$ is calculated from Eq. (11) (Fig. 9). $\varphi_{GB}(V)$ measured directly is also plotted in Fig. 8 for comparison, which confirms that the behavior of a biased *GB* is consistent with the double Schottky barrier model.

In contrast to Sample A, the resistance anomaly in Sample B occurred around $T_{MAX} = 40$ K, (Fig. 10(a)). Surface potential images of the *GB* under zero bias were acquired at 30 K, 98 K and 293 K. As shown in Fig. 10(b), the potential barrier height at 30 K is significantly reduced compared to that measured at 98 K and 293 K, which are above the transition. This indicates that the sharp decrease in resistance below $T_{MAX} =$

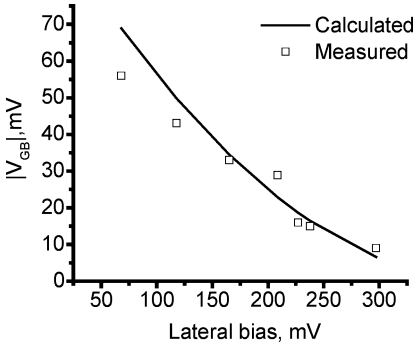

Fig. 9 The trend of decreasing magnitude of V_{GB} with increasing lateral bias V is close to that calculated from Eq. (4), which indicates the consistence with the double Schottky barrier model

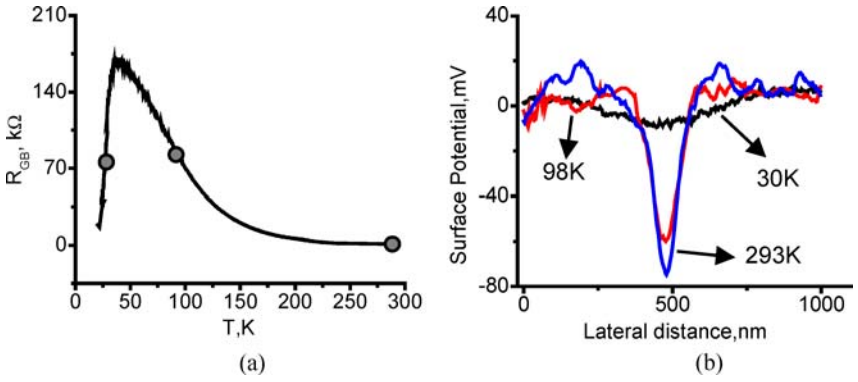

Fig. 10 (a) Potential profiles of the *GB* in Sample B were acquired at 30, 98 and 293 K. (b) Measured V_{GB} at these temperatures are −15 mV, −65 mV and −100 mV respectively. The significant diminution of potential at 30 K is consistent with the postulated PTCR effect

40 K is accompanied by a decrease in barrier height, in support of the boundary charge compensation by dielectric polarization. Furthermore, the T_{MAX} in Sample B is much lower than that of Sample A, which is probably due to the difference in the average electric field $\bar{E}$ in the respective GBs. As the *GB* is cooled, the increase in dielectric constant and the final appearance of ferroelectric polarization both contribute to the decrease of $\bar{E}$. Thus with $\bar{E}$ at 293 K available for both samples, we are able to give the upper limits of T_C. According to the formalism in [23], polarization P is proportional to the expectation of pseudo-spin $<S^z>$ in the two-level Ising model, and the susceptibility χ is given by $\chi = \frac{P(E)-P(E-\Delta E)}{\varepsilon_0 \Delta E}$, where E is electric field. On the other hand, T_C is the temperature at which χ reaches the maximum value. Thus T_C can be equivalently determined from the temperature dependence of $<S^z>(E)$-$<S^z>(E-\Delta E)$. Here $<S^z>$ under a given field E and temperature T is numerically solved from

$$<S^z> = \frac{1}{2}\frac{J_0 <S^z> + 2\mu E}{H} \tanh\left(\frac{H}{2kT}\right) \tag{12}$$

where $H = \sqrt{\Omega^2 + (J_0 < S^Z > +2\mu E)^2}$, $J_0 = k \times 145$ K, $\Omega = 87$ K and $\mu = 12$ eÅ. In our calculation, E is equal to $\bar{E}$ and ΔE is chosen to be 1 V/mm, which is much smaller than $\bar{E}$. As shown in Fig. 11, the upper limits of T_C's are 220 and 130 K for Sample A and B, respectively. This is a very coarse estimate especially for Sample B, in which case the true T_C should be no higher than 40 K. Using room temperature value of $\bar{E}$ is an overestimation because $\bar{E}$ is not an externally applied field but is caused by *GB* charge, which means $\bar{E}$ is not temperature independent but becomes smaller at low temperature due to increased dielectric screening in $SrTiO_3$.

Finally, we should point out that finite temperature polar state at $SrTiO_3$ GBs could also be due to the lattice stress in the dislocation core. Stress-induced ferroelectricity in $SrTiO_3$ was first reported by Uwe et al. [24] and most recently demonstrated on strain thin films [25]. However, if stress is the sole origin of ferroelectricity, it is difficult to explain the significant difference in T_C in the two samples, which are of the same structure in the dislocation core.

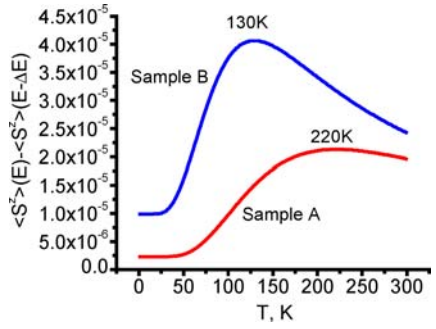

Fig. 11 Using built-in electric field at 293 K, temperature dependence of $<S^z>(E)-<S^z>(E-\Delta E)$ for both samples are calculated by solving Eq. 6. T_C, which corresponds to the peak in the temperature dependence of $<S^z>(E)-<S^z>(E-\Delta E)$, should be regarded as the upper limit of Curie temperature. For Sample A, this value is 220 K, and for sample B it is 130 K

6 Summary

In summary, we used two scanning potentiometry approaches and scanning impedance microscopy based on NC-AFM to characterize low temperature electrical transport properties of two 0.05 wt.% Nb-doped 24° $SrTiO_3$ GBs. We showed that the observed *GB* resistance anomaly at low temperatures is accompanied by typical PTCR behaviors of boundary potential barrier height decrease and boundary charge screening, indicating a low temperature ferroelectric-like phase transition at the GBs. This ferroelectric phase transition is ascribed to the large built-in electric field associated with the boundary charge and a numerical approach was employed to explain the difference in the two GBs.

Acknowledgments The authors gratefully acknowledge the financial support from DOE Grant DE-FG02-00ER45813-A001 and NSF Grant DMR03-04531. Discussions with Dr. Juraj Vavro (formerly with UPenn) and Dr. Jürgen Koeble (Omicron) are greatly appreciated.

References

1. L.M. Levinson (ed) *Electronic Ceramics: Properties, Devices and Applications*, (Marcel Dekker Inc., New York, 1988).
2. M.M. McGibbon, N.D. Browning, M.F. Chisholm, A.J. McGibbon, S.J. Pennycook, V. Ravikumar, and V.P. Dravid, *Science*, **266**, 102 (1994).
3. M. Kim, G. Duscher, N.D. Browning, K. Sohlberg, S.T. Pantelides, and S.J. Pennycook, *Phys. Rev. Lett*., **86**, 4056 (2001)
4. Z. Zhang, W. Sigle, W. Kurtz, and M. Rühle, *Phys. Rev*., **B 66**, 214112 (2002).
5. J. Petzelt, T. Ostapchuk, I. Gregora, et al., *Phys. Rev*., **B 64**, 184111 (2001).
6. D.A. Bonnell and S.V. Kalinin, *Z. Metallkd*., **94**, 188 (2003).
7. R. Shao, J. Vavro, and D.A. Bonnell, *Appl. Phys. Lett*., **85**, 561 (2004).
8. R. Shao, M.F. Chisholm, G. Duscher, and D.A. Bonnell, *Phys. Rev. Lett*., **95**, 197601 (2005).
9. B.D. Huey and D.A. Bonnell, *Solid State Ionics*, **131**, 51 (2000).
10. S.V. Kalinin and D.A. Bonnell, *Phys. Rev*., **B 62**, 10419 (2000).
11. S.V. Kalinin and D.A. Bonnell, *Nano Lett*., **4**, 555 (2004).
12. G.E. Pike and C.H. Seager, *J. Appl. Phys*., **50**, 3414 (1979).
13. K.A. Müller and H. Burkard, *Phys. Rev*., **B 19**, 3593 (1979).
14. H.-M. Christen, J. Mannhart, E.J. Williams, and C. Gerber, *Phys. Rev*., **B 49**, 12095 (1994).
15. H.-CH. Li, W. Si, A.D. West, and X.X. Xi, *Appl. Phys. Lett*., **73**, 464 (1998).
16. S. Kitamura and M. Iwatsuki, *Appl. Phys. Lett*., **72**, 3154 (1998).
17. R. Shao and D.A. Bonnell, *Appl. Phys. Lett*., **85**, 4968 (2004).
18. S.V. Kalinin and D.A. Bonnell, *J. Appl. Phys*., **91**, 832 (2002).
19. H.A. Sauer and J.R. Fischer, *J. Am. Ceram. Soc*., **43**, 297 (1960).
20. W.Heywang, *Solid State Electron*., **3**, 51(1961).
21. G.H. Jonker, *Solid State Electron*., **7**, 895(1964).
22. J. Hemberger, P. Lunkenheimer, R. Viana, R. Böhmer, and A. Loidl, *Phys Rev*., **B 52**, 13159 (1995).
23. J.G. Simmons, *J. Appl. Phys*. **34**, 1793 (1963).
24. H. Uwe and T. Sakudo, *Phys. Rev*., **B 13**, 271 (1976).
25. O. Tikhomirov, H. Jiang, and J. Levy, *Phys. Rev. Lett*., **89**, 147601(2002); J.H. Haeni, P. Irvin, W. Chang, et al., *Nature*, **430**, 758 (2004).